Atmos. Chem. Phys. Discuss., 14, 32177–32231, 2014
www.atmos-chem-phys-discuss.net/14/32177/2014/
doi:10.5194/acpd-14-32177-2014

Atmospheric Chemistry and Physics Discussions

Using the OMI Aerosol Index and Absorption Aerosol Optical Depth to evaluate the NASA MERRA Aerosol Reanalysis

V. Buchard[1,2], A. M. da Silva[1], P. R. Colarco[1], A. Darmenov[1], C. A. Randles[1,3], R. Govindaraju[1,4], O. Torres[1], J. Campbell[5], and R. Spurr[6]

[1]NASA/Goddard Space Flight Center, Greenbelt, MD, USA
[2]GESTAR/Universities Space Research Association, Columbia, MD, USA
[3]GESTAR/Morgan State University, Baltimore, MD, USA
[4]Science Systems and Applications, Inc, Lanham, MD, USA
[5]Marine Meteorology Division, Naval Research Laboratory, Monterey, CA, USA
[6]RT Solutions, Inc., 9 Channing Street, Cambridge, MA 02138, USA

Received: 23 October 2014 – Accepted: 25 November 2014 – Published: 19 December 2014

Correspondence to: V. Buchard (virginie.j.buchard-marchant@nasa.gov)

Published by Copernicus Publications on behalf of the European Geosciences Union.

Abstract

A radiative transfer interface has been developed to simulate the UV Aerosol Index (AI) from the NASA Goddard Earth Observing System version 5 (GEOS-5) aerosol assimilated fields. The purpose of this work is to use the AI and Aerosol Absorption Optical Depth (AAOD) derived from the Ozone Monitoring Instrument (OMI) measurements as independent validation for the Modern Era Retrospective analysis for Research and Applications Aerosol Reanalysis (MERRAero). MERRAero is based on a version of the GEOS-5 model that is radiatively coupled to the Goddard Chemistry, Aerosol, Radiation, and Transport (GOCART) aerosol module and includes assimilation of Aerosol Optical Depth (AOD) from the Moderate Resolution Imaging Spectroradiometer (MODIS) sensor. Since AI is dependent on aerosol concentration, optical properties and altitude of the aerosol layer, we make use of complementary observations to fully diagnose the model, including AOD from the Multi-angle Imaging Spectro-Radiometer (MISR), aerosol retrievals from the Aerosol Robotic Network (AERONET) and attenuated backscatter coefficients from the Cloud-Aerosol Lidar and Infrared Pathfinder Satellite Observation (CALIPSO) mission to ascertain potential misplacement of plume height by the model. By sampling dust, biomass burning and pollution events in 2007 we have compared model produced AI and AAOD with the corresponding OMI products, identifying regions where the model representation of absorbing aerosols was deficient. As a result of this study over the Saharan dust region, we have obtained a new set of dust aerosol optical properties that retains consistency with the MODIS AOD data that were assimilated, while resulting in better agreement with aerosol absorption measurements from OMI. The analysis conducted over the South African and South American biomass burning regions indicates that revising the spectrally-dependent aerosol absorption properties in the near-UV region improves the modeled-observed AI comparisons. Finally, during a period where the Asian region was mainly dominated by anthropogenic aerosols, we have performed a qualitative analysis

ACPD
14, 32177–32231, 2014

in which the specification of anthropogenic emissions in GEOS-5 is adjusted to provide insight into discrepancies observed in AI comparisons.

1 Introduction

The concept of the UV Aerosol Index (AI) was first introduced in the context of observations made by the Total Ozone Mapping Spectrometer (TOMS) sensors in the late 1990s (Herman et al., 1997; Torres et al., 1998), and has since been extended to apply to measurements with the Ozone Monitoring Instrument (OMI). It is a useful qualitative parameter for detecting the presence of absorbing aerosols in the atmosphere, based on a spectral contrast method in the near UV region where ozone absorption is very small (Herman et al., 1997; Torres et al., 1998, 2007). One interesting aspect of this parameter is that it is directly derived from instrument measurements, and consequently is not affected by uncertainties in assumed aerosol properties. Using AI for detecting aerosol has been applied to other sensors such as GOME (de Graaf et al., 2005) and SCIAMACHY (de Graaf and Stammes, 2005; Penning de Vries et al., 2009) and models (Colarco et al., 2002; Ginoux and Torres, 2003; Yoshioka et al., 2005). In these model studies, simulations of AI and Aerosol Optical Depth (AOD) were performed for dust plume cases and compared to corresponding observations in order to validate the model and constrain the model optical properties of dust aerosols.

The effect of aerosol on the climate system depends on the total aerosol concentration and the aerosol radiative or optical properties, particularly absorption. In this study, we use OMI measurements as independent validation of the UV aerosol absorption in the recent version of the Modern Era Retrospective analysis for Research and Applications aerosol reanalysis (MERRAero). While MERRAero includes assimilation of AOD from the Moderate Resolution Imaging Spectroradiometer (MODIS) instrument on both Terra and Aqua satellites, it does not assimilate any data capable of directly constraining its Aerosol Absorption Optical Depth (AAOD). Therefore, we use independent OMI observations to assess the quality of MERRAero's AAOD. In addition to comparisons to

ACPD
14, 32177–32231, 2014

OMI retrieved AAOD we perform an explicit radiative transfer calculation to simulate the UV AI from assimilated aerosol fields at OMI observation locations as another device for assessing absorption in MERRAero.

The sensitivity of the UV AI to aerosol concentration, optical properties and the aerosol layer height is well documented (Herman et al., 1997; Torres et al., 1998; Hsu et al., 1999; Mahowald and Dufresne, 2004; de Graaf et al., 2005). Hence, we extend our analysis by using several space-based and ground-based datasets to fully diagnose MERRAero, including AOD from MODIS and the Multi-angle Imaging SpectroRadiometer (MISR) sensors, as well as absorption optical depth retrievals from the AErosol RObotic NETwork (AERONET). By simulating the attenuated backscatter coefficient at 532 nm, we also use measurements from the Cloud-Aerosol Lidar and Infrared Satellite Observations (CALIPSO) mission to characterize the vertical placement of the aerosol plume in our system. In Sect. 2, we summarize the GEOS-5 aerosol modeling and data assimilation system. Section 3 briefly describes all data products used in this study. The methodology used to simulate AI from aerosol assimilated fields appears in Sect. 4. In Sect. 5 we first assess the quality of MERRAero AOD by doing comparisons to MODIS, MISR and AERONET retrievals, followed by the evaluation of the vertical distribution with CALIPSO measurements. Finally, MERRAero absorption is evaluated against OMI measurements over regions of particular interest. Concluding remarks appear in Sect. 6.

2 GEOS-5 and the MERRA Aerosol Reanalysis (MERRAero)

MERRA (Rienecker et al., 2011) is a NASA meteorological reanalysis for the satellite era using a major new version of the Goddard Earth Observing System Data Assimilation System Version 5 (GEOS-5), the latest version from the NASA Global Modeling and Assimilation Office (GMAO). The project focuses on historical analyses of the hydrological cycle for a broad range of weather and climate time scales, and places the NASA Earth Observing System (EOS) suite of observations in a climate context.

ACPD
14, 32177–32231, 2014

The MERRA time period covers the modern era of remotely sensed data, from 1979 through the present, with special focus of the atmospheric assimilation on the hydrological cycle. Like similar reanalyses, MERRA provides meteorological parameters (winds, temperature, humidity), along with a number of other diagnostics such as surface and top of the atmosphere fluxes, diabatic terms and the observational corrections imposed by the data assimilation procedure.

As a step toward an Integrated Earth System Analysis (IESA), the GMAO is producing several parallel reanalyses of other components of the earth system such as ocean, land and atmospheric composition. Of particular relevance for this paper is the MERRA Aerosol Reanalysis, where MODIS AOD observations are assimilated, providing a companion aerosol gridded dataset that can be used to study the impact of aerosols on the atmospheric circulation and air quality in general. Notice that MERRAero only covers the later years of MERRA, capitalizing on the improved aerosol measurements from NASA's EOS platforms. The key elements of GEOS-5 used for MERRAero are summarized below.

2.1 GEOS-5 overview

The Goddard Earth Observing System Version 5 (GEOS-5) earth system model, is a weather and climate capable model described in Rienecker et al. (2008). The GEOS-5 system includes atmospheric circulation and composition, oceanic and land components. By including an aerosol transport module based on the Goddard Chemistry, Aerosol, Radiation, and Transport model (GOCART, Chin et al., 2002), GEOS-5 provides the capability for studying atmospheric composition and aerosol-chemistry-climate interactions (Colarco et al., 2010). In addition to providing data assimilation of traditional meteorological parameters (winds, pressure and temperature fields, Rienecker et al., 2008), GEOS-5 includes assimilation of bias corrected AOD from MODIS from both Terra and Aqua satellites.

The GOCART module simulates five types of aerosols (dust, sea salt, black carbon (BC), organic carbon (OC) and sulfate) treated as external mixtures that do not interact

ACPD
14, 32177–32231, 2014

with each other. While dust and sea salt emissions are surface wind speed dependent, the others are prescribed from emissions inventories. The model includes loss processes, convective and large scale wet removal, dry deposition and sedimentation for dust and sea salt as well as chemical reaction to produce sulfate aerosol from oxidation of sulfur dioxide (SO_2).

GEOS-5 can be run in data assimilation or replay modes. In the data assimilation mode, a meteorological analysis is performed every six hours to constrain the meteorological state of the model. On the other hand, a replay mode uses a previous analysis to adjust the model's meteorological state (winds, temperature, specific humidity) much like a Chemical Transport Model (CTM). However, unlike a CTM, in GEOS-5 the aerosol transport dynamics are entirely consistent with the model thermodynamical state at every time step between analysis updates.

2.2 Data assimilation in GEOS-5

GEOS-5 features a mature atmospheric data assimilation system that builds upon the Grid-point Statistical Interpolation (GSI) algorithm jointly developed with the National Centers for Environmental Prediction (NCEP) (Wu et al., 2002; Derber et al., 2003; Rienecker et al., 2008). The GSI solver was originally developed at NCEP as a unified 3-Dimensional Variational (3-D-Var) analysis system for supporting global and regional models. GSI includes all the in-situ and remotely sensed data used for operational weather prediction at NCEP.

GEOS-5 also includes assimilation of AOD observations from the MODIS sensor on both Terra and Aqua satellites. This algorithm involves cloud screening and homogenization of the observing system by means of a Neural Net scheme that translates cloud-cleared MODIS reflectances into AERONET calibrated AOD (referred to hereafter as "MODIS NNR", where NNR refers to a Neural Net-derived retrieval). Based on the work of Zhang and Reid (2006) and Lary et al. (2010), we originally developed a back-propagation neural network to correct observational biases in MODIS operational retrievals. Later this system evolved into a neural net type of retrieval. In

ACPD
14, 32177–32231, 2014

this system, reflectances (instead of retrieved AOD) provide the main input, alongside solar and viewing geometry, MODIS cloud cover, climatological surface albedo and model derived surface wind speed. On-line quality control is performed with the adaptive buddy check of Dee et al. (2001), with observation and background errors estimated using the maximum likelihood approach of Dee and da Silva (1999). The AOD analysis in GEOS-5 is performed by means of analysis splitting. First, a 2-D analysis of AOD is performed using error covariances derived from innovation data. The 3-D analysis increments of aerosol mass concentration are then computed using an ensemble formulation for the background error covariance. In MERRAero, as well as in the GEOS-5 near real-time system, this calculation is performed using the Local Displacement Ensemble (LDE) methodology under the assumption that ensemble perturbations represent misplacements of the aerosol plumes. These ensemble perturbations are generated with full model resolution, without the need for multiple model runs.

2.3 GEOS-5 configuration for MERRAero

The MERRAero experiment covers the period 2002–2014 and was performed at $0.5^{\circ} \times 0.625^{\circ}$ latitude by longitude with 72 vertical layers between the surface and about 80 km. GEOS-5 was run in replay-mode using 6-hourly atmospheric analyses from MERRA (Rienecker et al., 2011) to update the meteorological state, with a full aerosol assimilation performed every 3 h. Note that wind stress, convective mass flux, etc, are explicitly computed by the model parameterizations and not provided by MERRA. Parameterizations of natural and anthropogenic emissions in MERRAero reflect several noteworthy updates compared with the previous version of the GEOS modeling system (Colarco et al., 2010). Emissions of SO_2 from anthropogenic sources come from the Emission Database for Global Atmospheric Research (EDGAR) Version 4.1 inventory, and the injection scheme was modified to account for the differences in injection profiles of emission sources from energy and non-energy sectors (Buchard et al., 2014). Biomass burning emissions are from the NASA Quick Fire Emission Dataset (QFED)

ACPD
14, 32177–32231, 2014

Version 2.1. QFED is a global fire radiative power based inventory of daily emissions of aerosol precursors and trace gases (Darmenov and da Silva, 2014). Production of sea-salt aerosols follows the Gong (2003) formulation of size dependent number flux, but with a modified windspeed term equal to $u_*^{2.41}$, where u_* is the friction velocity. A new independently derived sea surface temperature (SST) correction term was applied to modulate the strength of sea-salt emissions, as suggested by Jaegle et al. (2011).

3 Independent observations used for validation

3.1 AERONET

AERONET is a global ground-based network of automatic sunphotometers (Holben et al., 1998) that measure direct sun and sky radiances at several wavelengths. AOD are obtained from direct sun measurements with an accuracy to within ±0.015. An inversion algorithm provides Single Scattering Albedo (SSA) using the sky radiance measurements along the solar principal plane and along the solar almucantar (Dubovik et al., 2000; Dubovik and King, 2000). The uncertainty in the retrieved SSA varies between 0.03 and 0.07 depending on the aerosol type and loading. In our study, we used cloud-screened Level 2.0 data (quality assured). In Level 2.0, SSA is only retrieved for AOD greater than 0.4.

3.2 MISR Aerosol Retrievals

The Multi-angle Imaging Spectroradiometer flying on the Terra spacecraft uses multiple camera views to retrieve multi-spectral aerosol optical properties at 16 km × 16 km spatial resolution, including AOD and layer height under certain condition with about eight-day global coverage. MISR's multi-angle capability allows for aerosol characterization and retrievals over bright surfaces (Kahn et al., 2005). The MISR aerosol products version 22 are used in the comparisons.

ACPD
14, 32177–32231, 2014

3.3 OMI Aerosol products

OMI is a Dutch/Finnish instrument onboard the NASA EOS Aura spacecraft (Levelt et al., 2006) launched in July 2004. OMI is the successor of the TOMS instruments and is dedicated to the monitoring of the Earth's ozone, air quality and climate. It measures the solar light scattered by the atmosphere in the 270–500 nm wavelength range with a spatial resolution varying from 13 km × 24 km at nadir to about 28 km × 150 km along its scan edges. The UV-AI retrieval is derived from the near-UV aerosol retrieval algorithm (OMAERUV) described in detail in Torres et al. (2007). In addition to AI, OMI measured reflectances at 354 and 388 nm are used to derive AOD and AAOD at 388 nm. The OMAERUV algorithm uses pre-computed top of the atmosphere (TOA) reflectances for a set of 21 aerosol models composed of three aerosol types (dust, carbonaceous aerosols and sulfate-based aerosols) to retrieve AOD and AAOD. As the retrieval algorithm is sensitive to aerosol layer height, climatological aerosol vertical profiles derived from CALIPSO observations are used as a constraint (Torres et al., 2013). The surface albedo is assumed to be Lambertian and is given by a revisited TOMS-based monthly climatology that takes into account the spectral dependence in the range 331–380 nm (Torres et al., 2013). In our comparison, we use the Level 2 aerosol data products Version 1.4.2 for both AI and AAOD (OMAERUV readme file, 2011), except over regions dominated by carbonaceous aerosols, where we use an AAOD product derived from a research version (Torres et al., 2013). In order to account for sub-pixel cloud contamination, we use only the best data values corresponding with an algorithm quality flag equal to 0.

3.4 CALIOP

The Cloud Aerosol Lidar with Orthogonal Polarization (CALIOP), carried by CALIPSO as part of the NASA A-Train (Winker et al., 2007, 2009) since 2006, adds important information about the aerosol vertical structure. We used CALIOP data processed by the Naval Research Laboratory (NRL) adapted for their data assimilation application. More

ACPD
14, 32177–32231, 2014

precisely, we used attenuated backscatter CALIOP profiles that have been quality-assured and cloud-cleared and then averaged to a 1° latitude along-track segments and 100 m vertically during nighttime and 400 m during daytime (Campbell et al., 2010).

4 GEOS-5 Aerosol Index Simulator

Simulations of AI were performed from GEOS-5 assimilated aerosol fields at OMI observation locations using the radiative transfer code VLIDORT (Vector LInearized Discrete Ordinate Radiative Transfer) described in Spurr (2006). The model produced AI were compared with corresponding OMI measurements for several months in 2007 characterized by a good sampling of dust and biomass burning events. In selecting the period of study, we chose to avoid the OMI row anomalies that have occurred since 2008. Furthermore, model-derived AAOD were compared with the corresponding OMI retrievals at 388 nm over the same period.

We have developed an interface between GEOS-5 aerosol assimilated fields and VLIDORT in order to simulate AI at the OMI footprint. VLIDORT is a vector radiative transfer code designed to calculate atmospheric transmittance and radiance for a wide range of atmospheric, geometric and spectral conditions (Spurr, 2006). VLIDORT uses the discrete ordinates method to solve the radiative transfer equation, and the vector mode was designed to perform computations of polarized radiances. The effects of polarization are included through the calculation of four components of the Stokes vector.

In our AI simulation process, each 3-D MERRAero aerosol concentration profile is first interpolated to the OMI observation location. These concentration profiles are then converted into vertical profiles of optical properties such as AOD, SSA, and components $P(\theta)$ of the scattering phase matrix using the Mie theory code of Wiscombe (1980) for all aerosol types with the exception of dust aerosols. Particle non-sphericity is presently included for the optical properties of dust aerosols only, using a spheroidal shape distribution after Dubovik et al. (2006) and the optical properties database from

ACPD
14, 32177–32231, 2014

Meng et al. (2010). Details of the implementation are included in Colarco et al. (2014). In the baseline model simulations, the refractive indices for each aerosol species are derived from the Optical Properties for Aerosols and Clouds (OPAC, Hess et al., 1998). These profiles of optical properties derived at 354 and 388 nm are then inputs into VLIDORT to produce TOA radiances and calculate AI at 354 nm for each OMI viewing geometry (as described in Eqs. 1–3). To characterize the radiative behavior of the surface, we use the Lambertian option in VLIDORT, specifying a TOMS-based surface albedo climatology, as in the OMAERUV algorithm.

The MERRAero simulation of AI is based on the definition of aerosol index,

$$\mathrm{AI} = -100\left[\log_{10}\left(\frac{I^{\mathrm{Model}}_{354}}{I^{\mathrm{calc(Ray)}}_{354}(R^{\mathrm{Model}}_{388*})}\right)\right], \quad (1)$$

where I^{Model}_{354} is the VLIDORT calculated TOA radiance at 354 nm using MERRAero aerosol concentrations, $I^{\mathrm{calc(Ray)}}_{354}$ is the TOA radiance calculated at 354 nm in absence of aerosols assuming $R^{\mathrm{Model}}_{388*}$, the adjusted Lambertian Equivalent Reflectivity (LER) at 388 nm. Thus is calculated with VLIDORT as:

$$R^{\mathrm{Model}}_{388} = \frac{I^{\mathrm{Model}}_{388} - I^{\mathrm{calc(Ray)}}_{388}}{T^{\mathrm{Ray}}_{388} + S^{\mathrm{Ray}}_{b388}\left(I^{\mathrm{Model}}_{388} - I^{\mathrm{calc(Ray)}}_{388}\right)}, \quad (2)$$

where T^{Ray}_{388} and S^{Ray}_{b388} are respectively the simulated transmittance and spherical albedo for a Rayleigh atmosphere, and

$$R^{\mathrm{Model}}_{388*} = R^{\mathrm{Model}}_{388} - \left(R^{\mathrm{sfc}}_{388} - R^{\mathrm{sfc}}_{354}\right) \quad (3)$$

with $R^{\mathrm{sfc}}_{\lambda}$ being the surface albedo values at λ and $R^{\mathrm{sfc}}_{388} - R^{\mathrm{sfc}}_{354}$ being a correction for the spectral dependence of the surface albedo.

ACPD
14, 32177–32231, 2014

An example of the comparison of monthly mean TOA radiances measured by OMI at 388 nm and our VLIDORT calculated radiances appears in Fig. 1. Globally, the model tends to simulate radiances in good agreement with OMI. However underestimation is noticed over desert regions (Saharan dust over land and transported over the Atlantic, Saudi Arabia region, Taklamakan desert in Asia and part of southern US).

5 Evaluating Aerosol Absorption in MERRAero

Figure 2 shows global comparisons of monthly averaged MERRAero simulated AI (middle) vs. OMI retrievals (top) for the months of July (left) and August (right) 2007, a period with a good sampling of dust and biomass burning events. The difference OMI minus MERRAero AI appears on the bottom row. Globally, MERRAero simulated AI captures major features of the global absorbing aerosol observations for both months, although the model tends to underestimate the AI over parts of North and South America and especially in the south African biomass burning region. In the north African dust region, we notice mainly an underestimation of MERRAero AI over dust sources, while for the dust plume over the Atlantic Ocean, MERRAero is mostly overestimated. In contrast, MERRAero AAOD (Fig. 3) are generally higher than the OMI retrievals, especially over dust regions, but also over biomass burning regions. In particular, MERRAero AI is underestimated in the presence of dust aerosols, while the AAOD is overestimated. In the African biomass burning region, MERRAero AI are very low compared with OMI AI, but MERRAero AAOD is overestimated, mostly over land.

In order to reconcile these conflicting diagnoses we choose four regions to evaluate MERRAero extinction, absorption and vertical distribution. For dust we choose an area over Sahara and the North Atlantic Ocean (60° W–20° E, 0–30° N) during the months of June through August 2007 (JJA). For biomass burning aerosol, we select two regions over South America (80–50° W, 30° S–10° N) and southern Africa (10° W–30° E, 0–30° S) to analyze during JJA 2007. Finally, we select an area over the Asian region

ACPD
14, 32177–32231, 2014

(70–130° E, 10–40° N) mainly dominated by anthropogenic aerosols during the period of April through June 2007 (AMJ).

5.1 Saharan dust aerosols

5.1.1 Dust optical depth

Figure 4 shows a comparison of MERRAero 550 nm AOD to MODIS NNR (top panel) and MISR observations (bottom panel) over the Saharan dust region during JJA 2007. The comparison with MODIS AOD includes only data from the Terra satellite that are coincident with MISR measurements. The model was sampled according to the time and location of such observations. Since a log-normal representation is more suitable to report AOD statistics (O'Neill et al., 2000), a kernel density estimation (KDE) (Silverman, 1986; Scott, 1992) was applied to approximate the joint probability density function (PDF) of observed and modeled logarithmic (natural) transformed AOD. The log-transformed AOD,

$$\eta = \log(\tau + 0.01), \tag{4}$$

where τ stands for AOD, is found to be closer to a normal distribution than simply $\log\tau$. The results in Fig. 4 (and later) are presented on a log-transformed scale.

The correlation coefficient r, the Root Mean Square of the differences (MERRAero-"observation"; RMS), the standard deviation of the differences (STDV) and the mean difference are calculated for logarithmically transformed AOD as summarized in Table 1. The comparison between simulated and observed AOD are very good with high correlation coefficient, 0.97 and 0.90 with MODIS NNR and MISR, respectively. As expected, MERRAero AOD agree better with the assimilated MODIS NNR (mean difference = 0.06) than with the indepedent MISR AOD (mean difference = −0.11) observations. Part of this bias may be explained by the tendency of MISR AOD to be overestimated over ocean compared with MODIS and AERONET, as noticed by Kahn et al. (2009, 2010), especially for low AOD below 0.25. If we consider only data over ocean,

ACPD
14, 32177–32231, 2014

the mean difference between MERRAero and MISR AOD becomes −0.18 while it is −0.08 over land.

In Fig. 5, we compare MERRAero AOD at 440 nm to available ground-based measurements from the AERONET network at several stations located in the Saharan region. We can see that MERRAero estimates of log-transformed AOD are well correlated ($r = 0.69$), but with a positive bias relative to AERONET measured AOD (the mean difference is equal to 0.20). (The right panel will be discussed in Sect. 5.1.4.)

5.1.2 Dust vertical structure

Figure 6 presents the JJA 2007 regional average of CALIOP 532 nm aerosols attenuated backscatter (left) and the corresponding attenuated backscatter sampled from the model (right) during day (top) and night (bottom). For the sake of comparison, the molecular scattering component was removed from the CALIOP profiles. MERRAero and CALIOP exhibit similar vertical structure, with a dust plume that extends up to 6 km for CALIOP and around 5 km for MERRAero over the Saharan region and descends as it travels west to the Caribbean over a shallow marine aerosol layer during day and night. According to Colarco et al. (2003), the general descent of air between Africa and the Caribbean, as well as particle sedimentation, might explain the descent of the plume. The MERRAero derived attenuated backscatter coefficient is in the same range as CALIOP, with a maximum value in the shallow marine aerosol layer over the Atlantic ocean. However, over land the model tends to have a higher aerosol concentration in the lowest atmospheric layers below 2 km compared with CALIOP. This concentration of aerosols in the lowest layers is even more pronounced during night.

5.1.3 Dust absorption

Figure 7 (top panel) shows comparisons of MERRAero simulated AI and that observed by OMI over Sahara and the North Atlantic dust region for the period JJA 2007. These baseline simulations are based on dust optical properties derived from the OPAC

ACPD
14, 32177–32231, 2014

database. A KDE was applied to approximate the PDF of observed and modeled AI. The AI simulation has been performed considering all aerosol types but the comparison is shown for only aerosols considered as dust by the model (the fraction of modeled AAOD due to dust aerosol is greater than 0.7).

The baseline MERRAero AI is well correlated with OMI AI ($r = 0.61$). However, there is considerable scatter, with a STDV of differences equal to 0.70. As seen in Fig. 2, this scatter is mainly due to the difference in AI behavior over land and ocean in this region. Over land, MERRAero AI is generally lower than OMI AI, while it is the opposite over ocean. The bottom plot of Fig. 7 shows the overestimation of MERRAero AAOD at 388 nm relative to OMI. We recall the AOD assimilation from MODIS places a constraint on the total aerosol loading, but does not constrain other relevant parameters, such as composition and optical properties of individual species. The PDF of the differences (MERRAero – OMI, not shown) indicates a bimodal distribution, with a majority of points (86 % of points) at differences lower than 2 (in log-space). For this mode, r is 0.53 and the mean difference is equal to 0.58. For the second mode, with differences greater than 2, the correlation coefficient is 0.51 and the mean difference is equal to 3.4.

5.1.4 Sensitivity analysis

The results so far have indicated that the baseline MERRAero simulation produces relatively good simulated AI, but an overestimation of MERRAero AAOD relative to OMI. In this subsection we explore the sensitivity of these results to the assumptions about dust optical properties. In the baseline simulation reported above, the dust refractive indices are from the OPAC database; these refractive indices are known to be highly absorptive (Fig. 7). In contrast, absorption estimates inferred from space-based remote sensing suggest dust is much less absorbing in the shortwave (Kaufman et al., 2001; Moulin et al., 2001; Colarco et al., 2002; Balkanski et al., 2007). As detailed in Colarco et al. (2014), an alternative set of refractive indices is derived from the observation-based database (referred to hereafter as “observation-based”) constructed from Colarco et al. (2002) in the UV, Kim et al. (2011) in the visible and Shettle and Fenn (1979)

ACPD
14, 32177–32231, 2014

in the infrared domain. This set of refractive indices shows a reduction of absorption compared with OPAC.

Adopting the observation-based dust optics results in a negative bias for AI (not shown) while the AAOD positive bias is reduced (note that the particle shape was kept the same). In addition to the change of the set of refractive index, we have increased the imaginary part of the refractive index at 354 nm and kept the refractive index at 388 nm constant. This modification of the dust optical properties follows the wavelength dependence of absorption in the near UV for dust aerosol used in the OMI OMAERUV algorithm (Torres et al., 2007) and retrieved from a laboratory study by Wagner et al. (2012). New comparisons of AI and AAOD at 388 nm assuming the observation-based optics and the absorption spectral contrast between 354 and 388 nm are presented in Fig. 8. While the AI comparison is quite similar to the baseline OPAC-based simulation, the MERRAero AAOD bias is much reduced relative to OMI. As noted previously, the PDF of the differences (MERRAero – OMI AAOD) has a bimodal distribution. For the mode with differences lower than 2 (88 % of points), r is now equal to 0.50 and the mean difference is equal to 0.10. For the second mode, with differences greater than 2, the correlation coefficient is 0.50 and the mean difference is equal to 3.2.

We now examine the impact of applying a new set of dust optics on MERRAero-derived AAOD by comparing it with AERONET retrievals. (Recall that the shortest wavelength for which AERONET retrievals of SSA is 440 nm.) As depicted in Fig. 5 (right panel) the optical properties derived from the OPAC-based simulations (in black) are generally more absorptive than the AERONET retrievals. MERRAero AAOD agrees better with AERONET retrievals when the observation-based dust optics tables (in green) are used. Figure S1, in the Supplemental, shows a comparison of MERRAero SSA against AERONET retrievals at 440 nm. Regardless of the dust optics used in the simulation, MERRAero SSA values have a much smaller range when compared to AERONET. This result underlines one of the limitations of bulk aerosols models such as GOCART: there is only one type of dust with a single mineralogy, and only external

ACPD
14, 32177–32231, 2014

mixtures are possible. In reality, dust of different sources have different mineralogy with varying amounts of iron and absorptive properties.

5.1.5 Impact of optical assumptions on dust aerosol direct radiative effect

We next analyze the effect of the updated dust optics on modeled direct aerosol effect during JJA 2007. Radiative forcing is calculated as the net flux change with and without aerosols. Defined this way, a positive TOA forcing indicates the addition of energy to the climate system (i.e. a radiative warming effect), whereas a negative effect indicates a net loss of energy (i.e., a radiative cooling effect) (e.g. Randles et al., 2013). TOA forcing is the sum of the atmospheric (ATM) and surface (SFC) forcing. Table 2 gives the JJA 2007 global shortwave (SW) clear-sky direct radiative effect (DRE) from all aerosols for the MERRAero baseline simulation and for a MERRAero experiment with the observation-based dust optical properties (noted as Obs). Also shown is the percent difference between the two experiments. The longwave clear sky radiative effect was the same for the two experiments (not shown). There is a 17 % decrease in the magnitude of the TOA SW DRE in the MERRAero-observation simulation while there is an increase of 5.6 % in the magnitude of the SFC SW DRE. Using less absorbing dust optical properties causes less warming in the atmosphere by about 20 %.

5.2 Biomass burning in Southern Africa and South America

5.2.1 Biomass burning aerosol optical depth

Here we focus our analysis on the two biomass burning regions in southern Africa and South America. As in the Saharan dust case, we have first compared MERRAero AOD at 550 nm against MODIS NNR and MISR retrievals. As expected, MERRAero AOD at 550 nm agrees well with the MODIS NNR retrieval, regardless of the region (shown as supplemental Fig. S2). Figure 9 shows comparisons against MISR, similar to Fig. 4 (bottom panel), but for southern Africa (top panel) and South America (bottom panel).

ACPD
14, 32177–32231, 2014

These comparisons show high correlation ($r = 0.95$ and $r = 0.91$ for southern Africa and South America respectively). However, on average MERRAero AOD are lower than MISR AOD, except for the lowest AOD over South America (the mean difference are equal to −0.19 for southern Africa and −0.05 for South America). Such discrepancies can be traced to similar underestimation of the MODIS NNR AOD retrievals that were assimilated in MERRAero.

Figure 10 presents AOD comparisons at 440 nm at some AERONET ground-based sites over southern Africa. For this analysis we have used a longer period from June to October 2007 in order to increase the sample size. Similar comparisons over South America are presented in the Supplement as Fig. S3. For both regions, MERRAero AOD is well correlated with the observations ($r = 0.78$ for southern Africa and $r = 0.95$ for South America). However, like the negative bias observed with MISR at 550 nm, the model derived AOD at 440 nm exhibits a negative bias relative to AERONET (Mean difference = −0.27 and −0.20 for southern Africa and South America respectively). All statistics are summarized in Table 3.

5.2.2 Biomass burning aerosol vertical structure

As in the dust case, we have evaluated the MERRAero vertical distribution of aerosols over the biomass burning domain for day and night. Figure 11 shows comparisons between CALIOP and model-derived attenuated backscatter at 532 nm over southern Africa for the period of JJA 2007. The simulated attenuated backscatter signal of MERRAero is of the same order of magnitude as the CALIOP estimates, except for marine layer aerosols where the MERRAero smoke plume appears to extend further offshore. The maximum attenuated backscatter coefficient in MERRAero is shifted during the daytime, peaking at longitude range 5 and 12° E while CALIOP maximum values are between 25 and 30° E. During night, the maximum occurs for both CALIOP and MERRAero over the continent between 15–25° W. The GEOS-5 smoke plume is displaced west of the continent, tending to downward gradually over the marine aerosols from 15 to 0° E, while elevated aerosols are not found in the CALIOP profiles west of 12° E.

ACPD
14, 32177–32231, 2014

Several reasons may explain these discrepancies. First, the model dynamics exhibit strong subsidence west of the continent, contributing to downward transport of the smoke in this region that increases the likelihood of subsequent removal by precipitation in the marine cloud deck. Second, much like operational MODIS aerosol retrievals, the MODIS NNR retrievals have separate land and ocean algorithms, each using different channels and predictors. An analysis of the three month averaged AOD analysis increments over this region indicates that the assimilation tends to add more aerosol mass in the model over ocean than over land (not shown). Finally, the discontinuity observed in the CALIOP profiles between land and ocean could be due to the presence of low-level clouds over the Atlantic Ocean off southwestern Africa, which have caused a removal of some of CALIOP profiles during the screening process when the CALIOP data are averaged at $1^{\circ} \times 1^{\circ}$ horizontal resolution along-track. Over South America, the presence of clouds in the data profile can be difficult to screen out, making the comparisons harder to make in terms of magnitude of the attenuated backscatter coefficient. However, MERRAero vertical distribution compares well with the observations there (not shown).

5.2.3 Biomass burning aerosol absorption

Figure 12 shows comparisons of MERRAero and OMI AI and AAOD over the south African region. A similar comparison for the South American regions appears in the Supplement (Fig. S4). While all measurements were included in the simulation, for the comparison here we select only those measurements for which OC and BC are the predominant aerosols. Such condition is met when the fraction of MERRAero AAOD from OC and BC is greater than 0.7. The low values of r indicate a weak correlation between the modeled and measured AI ($r = 0.09$ and $r = -0.02$ for southern Africa and South America, respectively). The lack of aerosol microphysics and overly simplified aging processes for carbonaceous species in GOCART may account for MERRAero not capturing the true variability in SSA (e.g. Figs. S5 and S6). Besides the larger scatter, the MERRAero estimates of AI are lower than the observations regardless of

ACPD
14, 32177–32231, 2014

the region. One of the reasons for this AI underestimation is the MERRAero AOD low bias relative to MISR and AERONET seen in Sect. 5.2.1.

The bottom plots in Fig. 12 shows the AAOD comparison with OMI at 388 nm. The OMI AAOD used in these comparisons comes from a research version of the OMAERUV retrieval algorithm which has improved OMI retrievals of AOD and SSA, particularly for smoke aerosol (more details on the product can be found in Torres et al., 2013). While the MERRAero AAOD is underestimated over southern Africa, it is generally overestimated over South America (Fig. S4). The fact that MERRAero specifies the same optical properties of OC and BC over Africa and South America may not capture the diversity of smoke in these regions, and in turn account for this discrepancy.

Figure 10 (right panel) shows MERRAero AAOD against AERONET retrievals at 440 nm over few stations in southern Africa. This comparison confirms the same negative bias reported previously with OMI AAOD over a larger region (Fig. 12). Similar comparison over South America is shown on Fig. S3 (right panel). We find a positive bias for high values of AAOD and a negative bias for low AAOD values, which is, again, consistent with the OMI AAOD comparison (Fig. S4).

5.2.4 Sensitivity analysis

We now examine the effect of the absorption spectral dependence on the AI simulations. Generally speaking, wavelength-dependent aerosol absorption leads to increased AI (de Graaf et al., 2005; Jethva and Torres, 2011). Several studies (Kirchstetter et al., 2004; Bergstrom et al., 2007; Russell et al., 2010) show that the absorption for OC in biomass burning aerosols varies with wavelength in the UV and visible. In a way similar to the well-known Angstrom exponent, the Absorption Angstrom Exponent (AAE) is used to describe the spectral dependence of the AAOD. For BC, absorption is spectrally flat and AAE is estimated to be equal to 1.0 (Bond, 2001), while AAE is larger than 1.0 for OC aerosols in the UV regions. In the MERRAero baseline simulations, the absorption for biomass burning aerosols is spectrally flat, with an AAE close to 1 in the 350–400 nm range.

ACPD
14, 32177–32231, 2014

For biomass burning aerosols, Jethva and Torres (2011) found that OMI retrieved AOD compares better with AERONET observations when AAE varies between 2.5 and 3.0. Following this study, we performed two sensitivity analyses where we increased the spectral contrast in the absorption of our OC component of biomass burning. We did this by decreasing the SSA at 354 nm by 2 and 5 % while holding the SSA at 388 nm constant, yielding an AAE between 2.5 and 4.0. All the statistics resulting from this analysis are summarized in Table 4. Unlike the original comparison, the new comparison after decreasing the SSA by 5 % only for OC at 354 nm shows significantly improved agreement between modeled and observed AI over southern Africa (Fig. 13). The correlation coefficient increased from 0.09 to 0.65 and the absolute value of the mean difference decreased from −0.55 to 0.08. For the South American region, there is an improvement that is much less pronounced than over South Africa (not shown).

5.3 Anthropogenic aerosols in Asia

5.3.1 Asian aerosol optical depth

Figure 14 shows the model AOD at 550 nm vs. MISR over the Asian region for AMJ 2007. The comparison against MODIS NNR is shown on Fig. S7. Agreements are good, with both MODIS NNR and MISR with high correlation coefficient (r = 0.92 and r = 0.80) and very low bias (Mean difference = −0.018 and 0.015 relative to MODIS and MISR respectively). The comparison against AERONET retrievals at 440 nm is presented on Fig. 15. MERRAero AOD is well correlated with AERONET AOD (r = 0.87), but the model underestimates the retrievals except for a few measurements characterized by a very low AOD (mean difference = −0.16). All statistics are summarized in Table 5. This negative bias may be a consequence of emission deficiency in the model over the Asian region that cannot be overcome by AOD assimilation in an often cloudy region. Furthermore, AERONET comparisons are performed for all times with a value measurement, regardless of satellite overpass times. The model was run with SO_2 anthropogenic emission from the EDGAR version 4.1 dataset available for the year

ACPD
14, 32177–32231, 2014

2005, which is likely too low for the year 2007. Additionally, the nitrate particle formation is not considered in GEOS-5. Asian anthropogenic emissions continue to increase (Zang et al., 2009; Smith et al., 2011; Kiurokawa et al., 2013), with the most significant growth for Nitrogen Oxide (NO_x) emissions. China and India are the two most important contributors to Asian emissions (Zang et al., 2009; Kiurokawa et al., 2013) and the uncertainties in SO_2 emissions over China are large (Smith et al., 2011). SO_2 emissions significantly increased between 2001 and 2006 (Zang et al., 2009; Lamsal et al., 2011) and decreased from 2006 to 2010 from implementation of flue gas desulfurization in power plants (Lamsal et al., 2011; Kiurokawa et al., 2013). Nitrogen oxides (NO_x) emissions in China and more generally over East Asia have significantly increased from 2000 to 2008 (Zang et al., 2009; Lamsal et al., 2011; Kiurokawa et al., 2013).

5.3.2 Asian aerosol vertical structure

Figure 16 shows MERRAero attenuated backscatter coefficient compared with the CALIOP product averaged over the Asian region during the months AMJ 2007. We find that the vertical distribution is well represented in the model. However, as seen in the biomass burning region in southern Africa, the model tends to have more aerosols than the observation in the lowest layers of the atmosphere. Globally over the region, MERRAero produces the observed magnitude of attenuated backscatter coefficient.

5.3.3 Asian aerosol absorption

Figure 17 (top panel) shows the comparisons of AI simulated by the model and observed by OMI over the Asian region during the AMJ 2007. Only measurements with predominantly carbonaceous and sulfate aerosols are selected (the fraction of MERRAero AAOD from OC, BC and sulfate is greater than 0.7). We see that, contrary to the analysis performed over the biomass burning regions, MERRAero AI has a positive bias relative to OMI. On the bottom plot, MERRAero AAOD at 388 nm is overestimated

ACPD
14, 32177–32231, 2014

compared with the OMI retrieval (research product). If we look at the comparisons with AERONET retrievals at 440 nm (Fig. 15, right panel), we can see that the AAOD comparison looks better than the SSA comparison (Fig. S8). Compared with AERONET, MERRAero SSA tends to exhibit a low bias, except for the site of Ghandi-College (India).

5.3.4 Sensitivity analysis

Examining model emissions over the region, the month of April is dominated by biomass burning emissions while May and June are dominated by anthropogenic emissions. In order to shed some light on the MERRAero-AI positive bias relative to OMI, we perform here a qualitative sensitivity analysis. We focus on only one month (May), when the mean difference between MERRAero and OMI AI is equal to 0.31 and r equal to 0.50. As discussed previously, SO_2 anthropogenic emissions over Asia are highly uncertain and the 2005 dataset used in MERRAero may be too low for 2007. The assimilation of AOD constrains the total aerosol loading, and the error covariance specification is such that the analysis increments for each aerosol species are modulated by its mass fraction relative to other species. Therefore, if an aerosol specie is too low compared with the other species, the assimilation algorithm will not be able to properly adjust its mass.

In order to assess the impact of adjusting the aerosol speciation in our background field (a 3 h aerosol forecast) we have performed an experiment where we double the SO_2 anthropogenic emissions in MERRAero, effectively decreasing the ratio of carbonaceous/sulfate aerosols. This resulted in a decrease of the bias between modeled and observed AI. Besides SO_2, the other anthropogenic components in GEOS-5 are OC and BC, the latter of which is the main known absorbing aerosol component. We considered two cases, one where all carbonaceous aerosols are BC or all are OC. With all carbonaceous aerosols being BC, the MERRAero AI is dramatically overestimated while with all carbonaceous aerosols being OC, the modeled-AI is dramatically underestimated (not shown). This prescribed ratio of OC/BC emissions in MERRAero

ACPD
14, 32177–32231, 2014

is constant over the year while studies suggested that the mass of OC relative to BC should vary with the seasons (Arola et al., 2011; Lin et al., 2009) (note that these studies are performed over few local sites in Asia). In a final sensitivity experiment, we have increased OC and decreased BC emissions, resulting in a decrease of the bias between MERRAero and OMI AI. These sensitivity analyses underscore the need for reliable emission estimates, as well as for new instruments with sufficient information content as to constrain speciation and aerosol absorptive properties.

6 Conclusions

MERRAero assimilates MODIS aerosol measurements producing a time series of 3-D aerosol gridded fields for the Aqua period (mid-2002 to present). While the assimilated MODIS AOD does not constrain aerosol speciation, absorption properties or its vertical structure, the data assimilation system is capable of producing diagnostics of these unobserved quantities. This paper uses independent observations to validate these aerosol diagnostics, and in the process fine tune the aerosol optical properties assumed in the model.

By developing an interface between MERRAero aerosol fields and the radiative transfer code VLIDORT, we are able to simulate UV AI at OMI observation locations under clear sky conditions. Baseline monthly mean comparisons showed that MERRAero simulated AI were reasonable compared with OMI AI. However, MERRAero derived AAOD were overestimated compared to OMI retrievals at 388 nm. To shed some light on the reasons for this discrepancy, we have diagnosed factors determining AI: aerosol concentration, optical properties and aerosol layer height. We have stratified our analysis by regions characterized by different types of aerosols.

The evaluation of the AOD analysis over the Saharan dust region indicates good agreement with retrievals from MISR and a small positive bias relative to AERONET measurements, particularly over dust sources. The GEOS-5 dust plume height has a reasonable vertical structure compared with CALIOP. Comparisons of AAOD at

ACPD
14, 32177–32231, 2014

388 nm against OMI were improved using the observation-based dust optical properties of Colarco et al. (2014). This improvement was confirmed by comparison with AERONET AAOD retrievals. However, bringing MERRAero AI in agreement with OMI AI values required the introduction of an additional differential absorption between 354 and 388 nm.

Over biomass burning regions, MERRAero AOD are underestimated against MISR and AERONET data. In southern Africa, the vertical structure of MERRAero aerosol plume looks reasonable over land but appears to extend further over ocean compared with CALIOP data. MERRAero AAOD was underestimated in southern Africa and overestimated in South America; similar conclusions were confirmed by AERONET data. The large scatter noticed in SSA compared with AERONET emphasizes the difficulty simulating absorption optical properties from a bulk model like GOCART, where individual species (like BC and OC) have a fixed set of optical properties and where important aerosol microphysical processes are not taken into account. As a sensitivity analysis we have shown that introducing a wavelength-dependent aerosol absorption for OC can improve comparisons with OMI AI for smoke aerosols.

Over the Asian region, AOD comparisons show reasonable agreement with MISR AOD, with a slight underestimation compared to AERONET measurements. Sensitivity analysis reveals that adjusting anthropogenic emissions improves AI comparisons with OMI. The large scatter in SSA is consistent with a lack of microphysical processes in the model. Considering sub-speciation of dust and smoke particles may provide a pathway to improve scattering properties such as SSA. Over Asia, the uncertainties in anthropogenic emissions is another factor leading to uncertainties in speciation and therefore in absorption properties.

As a step towards improving the representation of aerosol microphysics in GEOS-5, the GMAO is currently implementing the Modal Aerosol Module (MAM) of Liu et al. (2012), coupled to the 2-moment cloud microphysical scheme described in Barahona et al. (2014). These improved model parameterizations will be complemented by an

ACPD
14, 32177–32231, 2014

Ensemble Kalman Filter aerosol data assimilation system aimed at extracting speciation and size information content available within multi-spectral UV-visible reflectances.

The Supplement related to this article is available online at doi:10.5194/acpd-14-32177-2014-supplement.

Acknowledgements. Author J. Campbell acknowledges the support of the Office of Naval Research Code 322 and NASA Langley Research Center Interagency Agreement RPO201422 on behalf of the CALIPSO Science Team.

References

Arola, A., Schuster, G., Myhre, G., Kazadzis, S., Dey, S., and Tripathi, S. N.: Inferring absorbing organic carbon content from AERONET data, Atmos. Chem. Phys., 11, 215–225, doi:10.5194/acp-11-215-2011, 2011. 32200

Barahona, D., Molod, A., Bacmeister, J., Nenes, A., Gettelman, A., Morrison, H., Phillips, V., and Eichmann, A.: Development of two-moment cloud microphysics for liquid and ice within the NASA Goddard Earth Observing System Model (GEOS-5), Geosci. Model Dev., 7, 1733–1766, doi:10.5194/gmd-7-1733-2014, 2014. 32201

Balkanski, Y., Schulz, M., Claquin, T., and Guibert, S.: Reevaluation of Mineral aerosol radiative forcings suggests a better agreement with satellite and AERONET data, Atmos. Chem. Phys., 7, 81–95, doi:10.5194/acp-7-81-2007, 2007. 32191

Bergstrom, R. W., Pilewskie, P., Russell, P. B., Redemann, J., Bond, T. C., Quinn, P. K., and Sierau, B.: Spectral absorption properties of atmospheric aerosols, Atmos. Chem. Phys., 7, 5937–5943, doi:10.5194/acp-7-5937-2007, 2007. 32196

Bond, T. C.: Spectral dependence of visible light absorption by carbonaceous particles emitted from coal combustion, Geophys. Res. Lett., 28, 4075–4078, doi:10.1029/2001GL013652, 2001. 32196

Buchard, V., da Silva, A. M., Colarco, P., Krotkov, N., Dickerson, R. R., Stehr, J. W., Mount, G., Spinei, E., Arkinson, H. L., and He, H.: Evaluation of GEOS-5 sulfur dioxide simulations

ACPD
14, 32177–32231, 2014

during the Frostburg, MD 2010 field campaign, Atmos. Chem. Phys., 14, 1929–1941, doi:10.5194/acp-14-1929-2014, 2014. 32183
Campbell, J. R., Reid, J. S., Westphal, D. L., Zhang, J., Hyer, E. J., Welton, E. J.: CALIOP aerosol subset processing for global aerosol transport model data assimilation, J. Sel. Topics Appl. Earth Observ. Remote Sens., 3, 203–214, 2010. 32186
Chin, M., Ginoux, P., Kinne, S., Torres, O., Holben, B., N., Duncan, B. N., Martin, R. V., Logan, J. A., Higurashi, A., and Nakajima, T: Tropospheric aerosol optical thickness from the GOCART model and comparisons with satellite and sun photometer measurements, J. Atmos. Sci., 59, 461–483, 2002. 32181
Colarco, P., Toon, O., Torres, O., and Rasch, P.: Determining the UV imaginary index of refraction of Saharan dust particles from Total Ozone Mapping Spectrometer data using a three-dimensional model of dust transport, J. Geophys. Res.-Atmos., 107, D16, doi:10.1029/2001JD000903, 2002. 32179, 32191
Colarco, P. R., Toon, O. B., Reid, J. S., Livingston, J. M., Russell, P. B., Redemann J., Schmid, B., Maring, H. B., Savoie, D., Welton, E. J., Campbell, J. R., Holben, B. N., and Levy, R.: Saharan dust transport to the Caribbean during PRIDE:2Transport, vertical profiles, and deposition in simulations of in situ and remote sensing observations, J. Geophys. Res. 108, 8590, doi:10.1029/2002JD002659, 2003. 32190
Colarco, P. R., da Silva, A., Chin, M., and Diehl, T.: On-line simulations of global aerosol distributions in the NASA GEOS-4 model and comparisons to satellite and ground- based aerosol optical depth, J. Geophys. Res., 115, D14207, doi:10.1029/2009JD012820, 2010. 32181, 32183
Colarco, P. R., Nowottnick, E. P., Randles, C. A., Yi, B., Yang, P., Kim, K.-M., Smith, J. A., and Bardeen, C. G.: Impact of radiatively interactive dust aerosols in the NASA GEOS-5 climate model: sensitivity to dust particle shape and refractive index, J. Geophys. Res.-Atmos., 119, 753–786, doi:10.1002/2013JD020046, 2014. 32187, 32191, 32201
Darmenov, A. and da Silva, A.: The Quick Fire Emissions Dataset (QFED) – Documentation of versions 2.1, 2.2 and 2.4, Technical Report, NASA, in preparation, 2014. 32184
de Graaf, M. and Stammes, P.: SCIAMACHY Absorbing Aerosol Index – calibration issues and global results from 2002–2004, Atmos. Chem. Phys., 5, 2385–2394, doi:10.5194/acp-5-2385-2005, 2005. 32179

ACPD
14, 32177–32231, 2014

de Graaf, M., Stammes, P., Torres, O., and Koelemeijer, R. B. A.: Absorbing Aerosol Index: sensitivity analysis, application to GOME and comparison with TOMS, J. Geophys. Res., 110, D01201, doi:10.1029/2004JD005178, 2005. 32179, 32180, 32196

Dee, D. and da Silva, A.: Maximum-likelihood estimation of forecast and observation error covariance parameters. Part I: Methodology, Mon. Weather Rev., 124, 1669–1694, 1999. 32183

Dee, D., Rukhovets, L., Todling, R., da Silva, A., and Larson, J.: An adaptive buddy check for observational quality control, Q. J. Roy. Meteor. Soc., 127, 2451–2471, 2001. 32183

Derber, J. C., Purser, R. J., Wu, W.-S., Treadon, R., Pondeca, M., Parrish, D., and Kleist, D., 2003: Flow-dependent Jb in a global grid-point 3-D-Var, Proceedings of the ECMWF annual seminar on recent developments in data assimilation for atmosphere and ocean, Reading, UK, 8–12 September 2003. 32182

Dubovik, O. and King, M.: A flexible inversion algorithm for retrieval of aerosol optical properties from sun and sky radiance measurements, J. Geophys. Res., 105, 20673–20696, 2000. 32184

Dubovik, O., Smirnov, A., Holben, B., King, M. D., Kaufman, Y. J., Eck, T. F., and Slutsker, I.: Accuracy assessments of aerosol optical properties retrieved from Aerosol Robotic Network (AERONET) Sun and Sky radiance measurements, J. Geophys. Res., 105, 9791–9806, 2000. 32184

Dubovik, O., Sinyuk, A., Lapyonok, T., Holben, B. N., Mishchenko, M., Yang, P., Eck, T. F., Volten, H., Munoz, O., Veihelmann, B., van der Zande, W. J., Leon, J.-F., Sorokin, M., and Slutsker, I.: Application of spheroid models to account for aerosol particle nonsphericity in remote sensing of desert dust, J. Geophys. Res., 111, D11208, doi:10.1029/2005JD006619, 2006. 32186

Ginoux, P. and Torres, O.: Empirical TOMS index for dust aerosol: applications to model validation and source characterization, J. Geophys. Res., 108, 4534, doi:10.1029/2003JD003470, 2003. 32179

Gong, S. L.: A parameterization of sea-salt aerosol source function for sub- and super-micron particles. Global Biogeochem. Cy., 17, 1097, doi:10.1029/2003GB002079, 2003 32184

Herman, J. R. and Celarier, E.: Earth surface reflectivity climatology at 340 and 380 nm from TOMS data, J. Geophys. Res., 102, 12059–12076, 1997.

Herman, J. R., Bhartia, P. K., Torres, O., Hsu, C., Seftor, C., and Celarier, E.: Global distribution of UV-absorbing aerosols from Nimbus 7/ TOMS data, J. Geophys. Res., 102, 16911–16922, 1997. 32179, 32180

ACPD
14, 32177–32231, 2014

Hess, M., Koepke, P., and Schult, I.: Optical properties of aerosols and clouds: the software package OPAC, B. Am. Meteorol. Soc., 79, 831–844, 1998. 32187
Holben, B. N., Eck, T., Slutsker, I., Tanre, D., Buis, J. P., Setzer, A., Vermote, E., Reagon, J. A., Kaufman, Y. J., Nakajima, T., Lavenu, F., Jankowiak, I., and Smirnov, A.: AERONET – A federated instrument network and data archive for aerosol characterization, Remote Sens. Environ., 66, 1–16, 1998. 32184
Hsu, N., Herman, J., Torres, O., Holben, B., Tanre, D., Eck, T., Smirnov, A., Chatenet, B., and Lavenu, F.: Comparisons of the TOMS aerosol index with Sun-photometer aerosol optical thickness: results and applications, J. Geophys. Res., 104, 6269–6279, 1999. 32180
Jethva, H. and Torres, O.: Satellite-based evidence of wavelength-dependent aerosol absorption in biomass burning smoke inferred from Ozone Monitoring Instrument, Atmos. Chem. Phys., 11, 10541–10551, doi:10.5194/acp-11-10541-2011, 2011. 32196, 32197
Jaeglé, L., Quinn, P. K., Bates, T. S., Alexander, B., and Lin, J.-T.: Global distribution of sea salt aerosols: new constraints from in situ and remote sensing observations, Atmos. Chem. Phys., 11, 3137–3157, doi:10.5194/acp-11-3137-2011, 2011. 32184
Kahn, R., Gaitley, B., Martonchik, J., Diner, D., Crean, K., and Holben, B.: Multiangle Imaging Spectroradiometer (MISR) global aerosol optical depth validation based on 2 years of coincident Aerosol Robotic Network (AERONET) observations, J. Geophys. Res., 110, D10S04, doi:10.1029/2004JD004706, 2005. 32184
Kahn, R. A., Nelson, D. L., Garay, M., Levy, R. C., Bull, M. A., Martonchik, J. V., Diner, D. J., Paradise, S. R., Hansen, E. G., and Remer, L. A.: MISR aerosol product attributes, and statistical comparison with MODIS, IEEE T. Geosci. Remote, 47, 4095–4114, 2009. 32189
Kahn, R. A., Gaitley, B. J., Garay, M. J., Diner, D. J., Eck, T. F., Smirnov, A., and Holben, B. N.: Multiangle Imaging SpectroRadiometer global aerosol product assessment by comparison with the Aerosol Robotic Network, J. Geophys. Res., 115, D23209, doi:10.1029/2010JD014601, 2010. 32189
Kaufman, Y., Tanré, D., Dubovik, O., Karnieli, A., and Remer, L.: Absorption of sunlight by dust as inferred from satellite and ground-based remote sensing, Geophys. Res. Lett., 28, 1479–1482, 2001. 32191
Kim, D., Chin, M., Yu, H., Eck, T. F., Sinyuk, A., Smirnov, A., and Holben, B. N.: Dust optical properties over North Africa and Arabian Peninsula derived from the AERONET dataset, Atmos. Chem. Phys., 11, 10733–10741, doi:10.5194/acp-11-10733-2011, 2011. 32191

ACPD
14, 32177–32231, 2014

Kirchstetter, T. W., Novakov, T., and Hobbs, P. V.: Evidence that the spectral dependence of light absorption by aerosols is affected by organic carbon, J. Geophys. Res., 109, D21208, doi:10.1029/2004JD004999, 2004. 32196

Kurokawa, J., Ohara, T., Morikawa, T., Hanayama, S., Janssens-Maenhout, G., Fukui, T., Kawashima, K., and Akimoto, H.: Emissions of air pollutants and greenhouse gases over Asian regions during 2000–2008: Regional Emission inventory in ASia (REAS) version 2, Atmos. Chem. Phys., 13, 11019–11058, doi:10.5194/acp-13-11019-2013, 2013. 32198

Lamsal, L. N., Martin, R. V., Padmanabhan, A., van Donkelaar, A., Zhang, Q., Sioris, C. E., Chance, K., Kurosu, T. P., and Newchurch, M. J.: Application of satellite observations for timely updates to global anthropogenic NO_x emission inventories, Geophys. Res. Lett., 38, L05810, doi:10.1029/2010GL046476, 2011. 32198

Lary, D., Remer, L. A., MacNeil, D., Roscoe, B., and Paradise, S.: Machine learning and bias correction of MODIS aerosol optical depth, IEEE Geosci. Remote S., 6, 694–698, doi:10.1109/LGRS.2009.2023605, 2010. 32182

Levelt, P. F., Hilsenrath, E., Leppelmeier, G. W., van den Oord, G. H. J., Bhartia, P. K., Tamminen, J., de Haan, J. F., and Veefkind, J. P.: Science objectives of the Ozone Monitoring Instrument, IEEE T. Geosci. Remote, 44, 1199–1208, doi:10.1109/TGRS.2006.872336, 2006. 32185

Lin, P., Hu, M., Deng, Z., Slanina, J., Han, S., Kondo, Y., Takegawa, N., Miyazaki, Y., Zhao, Y., and Sugimoto, N.: Seasonal and diurnal variations of organic carbon in $PM_{2.5}$ in Beijing and the estimation of secondary organic carbon, J. Geophys. Res., 114, D00G11, doi:10.1029/2008JD010902, 2009. 32200

Liu, X., Easter, R. C., Ghan, S. J., Zaveri, R., Rasch, P., Shi, X., Lamarque, J.-F., Gettelman, A., Morrison, H., Vitt, F., Conley, A., Park, S., Neale, R., Hannay, C., Ekman, A. M. L., Hess, P., Mahowald, N., Collins, W., Iacono, M. J., Bretherton, C. S., Flanner, M. G., and Mitchell, D.: Toward a minimal representation of aerosols in climate models: description and evaluation in the Community Atmosphere Model CAM5, Geosci. Model Dev., 5, 709–739, doi:10.5194/gmd-5-709-2012, 2012. 32201

Mahowald, N. M. and Dufresne, J.: Sensitivity of TOMS aerosol index to boundary layer height: implications for detection of mineral aerosol sources, Geophys. Res. Lett., 31, L03103, doi:10.1029/2003GL018865, 2004. 32180

Meng, Z., Yang, P., Kattawar, G. W., Bi, L., Liou, K. N., and Laszlo, I.: Single-scattering properties of tri-axial ellipsoidal mineral dust aerosols: a database for application to radiative

ACPD
14, 32177–32231, 2014

transfer calculations, J. Aerosol Sci., 41, 501–512, doi:10.1016/j.jaerosci.2010.02.008, 2010. 32187
Moulin, C., Gordon, H., Banzon, V., and Evans, R.: Assessment of Saharan dust absorption in the visible from SeaWiFS imagery, J. Geophys. Res., 106, 18239–18249, 2001. 32191
OMAERUV readme file: Retrieved from the AURA OMI website: http://disc.sci.gsfc.nasa.gov/Aura/data-holdings/OMI/, 2011. 32185
O'Neill, N. T., Ignatov, A., Holben, B. N., and Eck, T. F.: The lognormal distribution as a reference for reporting aerosol optical depth statistics: empirical tests using multi-year, multi-site AERONET sunphotometer data, J. Geophys. Lett., 27, 3333–3336, 2000. 32189
Penning de Vries, M. J. M., Beirle, S., and Wagner, T.: UV Aerosol Indices from SCIAMACHY: introducing the SCattering Index (SCI), Atmos. Chem. Phys., 9, 9555–9567, doi:10.5194/acp-9-9555-2009, 2009. 32179
Randles, C. A., Colarco, P. R., and Da Silva, A.: Direct and semi-direct aerosol effects in the NASA GEOS-5 AGCM: aerosol-climate interactions due to prognostic vs. prescribed aerosols, J. Geophys. Res.-Atmos., 118, 149–169, doi:10.1029/2012JD018388, 2013. 32193
Rienecker, M., Suarez, M. J., Todling, R., Bacmeister, J., Takacs, L., Liu, H.-C., Gu, W., Sienkiewicz, M., Koster, R. D., Gelaro, R., Stajner, I., and Nielsen, J. E.: The GEOS-5 Data Assimilation System-Documentation of Versions 5.0.1, 5.1.0, and 5.2.0., Technical Report Series on Global Modeling and Data Assimilation, 104606, 27, 2008. 32181, 32182
Rienecker, M., Suarez, M. J., Gelaro, R., Todling, R., Bacmeister, J., Liu, E., Bosilovich, M. G., Schubert, S. D., Takacs, L., Kim, G.-K., Bloom, S., Chen, J., Collins, D., Conaty, A., da Silva, A., Gu, W., Joiner, J., Koster, R. D., Lucchesi, R., Molod, A., Owens, T., Pawson, S., Pegion, P., Redder, C. R., Reichle, R., Robertson, F. R., Ruddick, A. G., Sienkiewicz, M., and Woollen, J.: MERRA – NASA's Modern-Era Retrospective Analysis for Research and Applications, J. Climate, 24, 3624–3648, doi:10.1175/JCLI-D-11-00015.1, 2011. 32180, 32183
Russell, P. B., Bergstrom, R. W., Shinozuka, Y., Clarke, A. D., DeCarlo, P. F., Jimenez, J. L., Livingston, J. M., Redemann, J., Dubovik, O., and Strawa, A.: Absorption Angstrom Exponent in AERONET and related data as an indicator of aerosol composition, Atmos. Chem. Phys., 10, 1155–1169, doi:10.5194/acp-10-1155-2010, 2010. 32196
Scott, D. W.: Multivariate Density Estimation: Theory, Practice, and Visualization, Wiley, 1992. 32189

ACPD
14, 32177–32231, 2014

Shettle, E. P. and Fenn, R. W.: Models for the aerosols of the lower atmosphere and effects of humidity variation on their optical properties, Air Force Geophysics Laboratory Tech. Rep., AFGL-TR-79-0214, 94 pp., Hanscom AFB, Massachusetts, USA, 1979. 32191

Silverman, B. W.: Density Estimation, Chapman and Hall, London, 1986. 32189

Smith, S. J., van Aardenne, J., Klimont, Z., Andres, R. J., Volke, A., and Delgado Arias, S.: Anthropogenic sulfur dioxide emissions: 1850–2005, Atmos. Chem. Phys., 11, 1101–1116, doi:10.5194/acp-11-1101-2011, 2011. 32198

Spurr, R. J. D.: VLIDORT: a linearized pseudo-spherical vector discrete ordinate radiative transfer code for forward model and retrieval studies in multilayer multiple scattering media, J. Quant. Spectrosc. Ra., 102, 316–342, doi:10.1016/j.jqsrt.2006.05.005, 2006. 32186

Torres, O., Bhartia, P. K., Herman, J. R., Ahmad, Z., and Gleason, J.: Derivation of aerosol properties from satellite measurements of backscattered ultraviolet radiation: theoretical basis, J. Geophys. Res., 103, 17099–17110, 1998. 32179, 32180

Torres, O., Tanskanen, A., Veihelmann, B., Ahn, C., Braak, R., Bhartia, P. K., Veefkind, P., and Levelt, P.: Aerosols and surface UV products from Ozone Monitoring Instrument observations: an overview, J. Geophys. Res., 112, D24S47, doi:10.1029/2007JD008809, 2007. 32179, 32185, 32192

Torres, O., Ahn, C., and Chen, Z.: Improvements to the OMI near-UV aerosol algorithm using A-train CALIOP and AIRS observations, Atmos. Meas. Tech., 6, 3257–3270, doi:10.5194/amt-6-3257-2013, 2013. 32185, 32196

Wagner, R., Ajtai, T., Kandler, K., Lieke, K., Linke, C., Müller, T., Schnaiter, M., and Vragel, M.: Complex refractive indices of Saharan dust samples at visible and near UV wavelengths: a laboratory study, Atmos. Chem. Phys., 12, 2491–2512, doi:10.5194/acp-12-2491-2012, 2012. 32192

Winker, D. M., Hunt, B. H., and McGill, M. J.: Initial performance assessment of CALIOP, Geophys. Res. Lett., 34, L19803, doi:10.1029/2007GL030135, 2007. 32185

Winker, D. M., Vaughan, M. A., Omar, A. H., Hu, Y., Powell, K. A., Liu, Z., Hunt, W. H., and Young, S. A.: Overview of the CALIPSO Mission and CALIOP Data Processing Algorithms, J. Atmos. Ocean. Tech., 26, 2310–2323, 2009. 32185

Wiscombe, W.: Improved Mie scattering algorithms, Appl. Optics, 19, 1505–1509, 1980. 32186

Wu, W.-S., Purser, R. J., and Parrish, D. F.: Three-dimensional variational analysis with spatially inhomogeneous covariances, Mon. Weather Rev., 130, 2905–2916, 2002. 32182

ACPD
14, 32177–32231, 2014

Yoshioka, M., Mahowald, N., Dufresne, J. L., and Luo, C.: Simulation of absorbing aerosol indices for African dust, J. Geophys. Res., 110, doi:10.1029/2004JD005276, 2005. 32179
Zhang, J. and Reid, J.: MODIS aerosol product analysis for data assimilation: assessment of over-ocean level 2 aerosol optical thickness retrievals, J. Geophys. Res., 111, D22207, doi:10.1029/2005JD006898, 2006. 32182
Zhang, Q., Streets, D. G., Carmichael, G. R., He, K. B., Huo, H., Kannari, A., Klimont, Z., Park, I. S., Reddy, S., Fu, J. S., Chen, D., Duan, L., Lei, Y., Wang, L. T., and Yao, Z. L.: Asian emissions in 2006 for the NASA INTEX-B mission, Atmos. Chem. Phys., 9, 5131–5153, doi:10.5194/acp-9-5131-2009, 2009. 32198

ACPD
14, 32177–32231, 2014

Table 1. Summary of AOD comparisons results with MODIS NNR, MISR and AERONET (*n* is the number of points; *r* is the correlation coefficient; RMS is the Root Mean Square of the differences; STDV is the standard deviation of the differences and BIAS is the mean difference of the log-transformed AOD.

	Saharan dust				
	n	*r*	STDV	RMS	BIAS
MODIS NNR	9655	0.97	0.13	0.15	0.06
MISR	9655	0.90	0.25	0.27	−0.11
AERONET	1278	0.69	0.45	0.40	0.20

ACPD
14, 32177–32231, 2014

Table 2. Global JJA 2007 clear-sky Aerosol Direct Radiative Effect ($W m^{-2}$) for MERRAero baseline and MERRAero updated with the observation-based dust optical properties.

	TOA SW	Atmos. SW	Surface SW
MERRAero	−2.91	4.36	−7.27
MERRAero-Obs	−3.41 (−17 %)	3.45 (−21 %)	−6.86 (+5.6 %)

ACPD
14, 32177–32231, 2014

Table 3. Same as Table 1 but for the South African and South American regions.

	South Africa					South America				
	n	*r*	STDV	RMS	BIAS	*n*	*r*	STDV	RMS	BIAS
MODIS NNR	161 096	0.98	0.09	0.10	0.05	100 000	0.96	0.22	0.22	0.001
MISR	161 096	0.95	0.16	0.25	−0.19	100 000	0.91	0.34	0.34	−0.05
AERONET	681	0.78	0.41	0.50	−0.27	981	0.95	0.32	0.37	−0.20

ACPD
14, 32177–32231, 2014

Table 4. Summary of AI comparison between MERRAero and OMI for the period JJA 2007 after a decrease of 2 %, 5 % of the SSA at 354 nm for OC only. The SSA at 388 nm stays constant.

	South Africa (n = 580 691 pts)				South America (n = 444 758 pts)			
	r	STDV	RMS	BIAS	r	STDV	RMS	BIAS
Baseline simulation	0.09	0.55	0.78	−0.55	−0.02	0.57	0.58	−0.09
SSA ($OC_{354\,nm}$) ↘ 2 %	0.54	0.44	0.53	−0.30	0.16	0.55	0.55	0.03
SSA ($OC_{354\,nm}$) ↘ 5 %	0.65	0.48	0.49	0.08	0.21	0.63	0.67	0.23

ACPD
14, 32177–32231, 2014

Table 5. Same as Table 1 for the Asian region.

			Asia		
	n	*r*	STDV	RMS	BIAS
MODIS NNR	68 841	0.92	0.28	0.28	−0.018
MISR	68 841	0.80	0.35	0.35	0.015
AERONET	986	0.87	0.42	0.44	−0.16

ACPD
14, 32177–32231, 2014

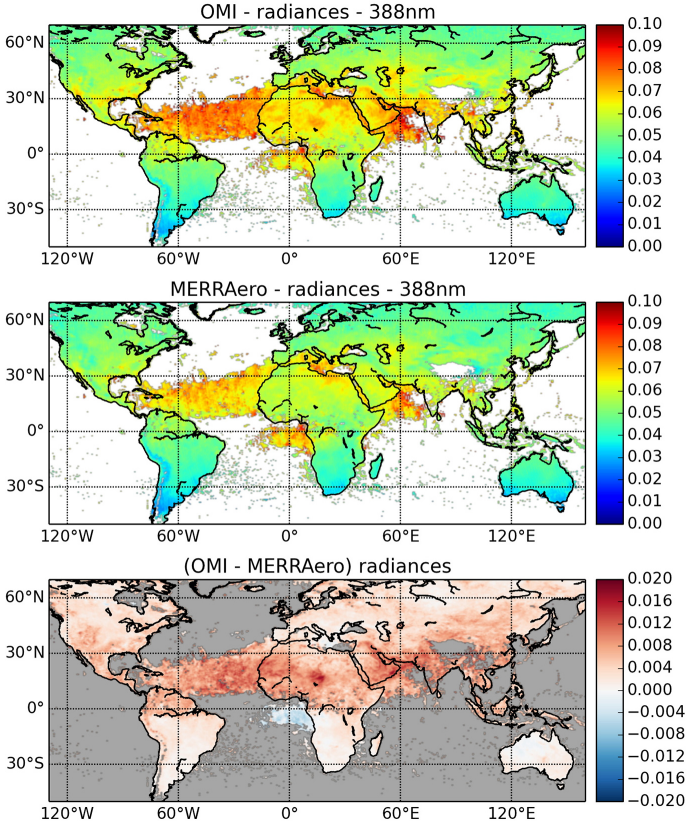

Figure 1. TOA monthly mean radiances at 388 nm observed by OMI (top) and calculated with VLIDORT using MERRAero aerosol fields (middle). Difference of radiances OMI minus MERRAero (bottom).

ACPD
14, 32177–32231, 2014

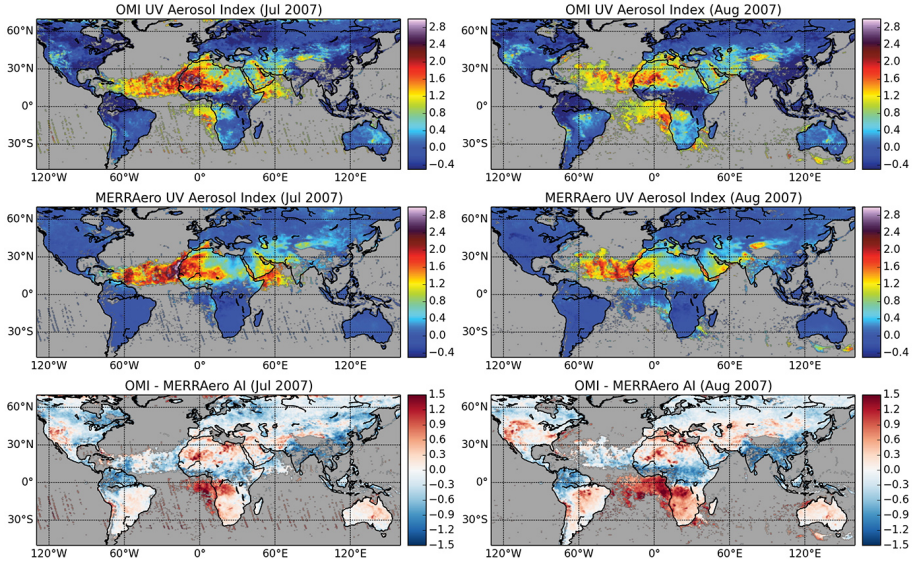

Figure 2. Monthly mean of OMI UV AI (top) and MERRAero simulated AI (middle) for July (left) and August (right) 2007. Difference of AI OMI minus MERRAero (bottom plots).

ACPD
14, 32177–32231, 2014

Using OMI AI and AAOD to evaluate MERRAero absorption

V. Buchard et al.

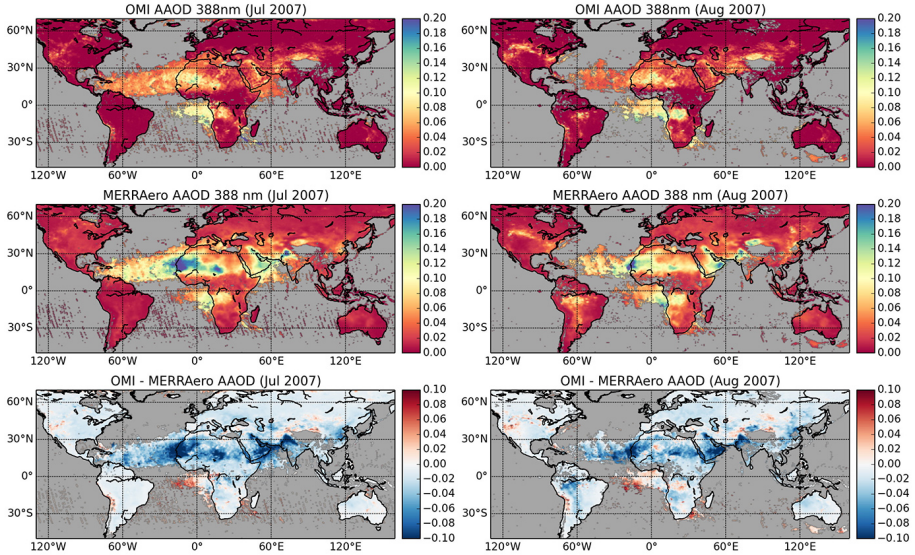

Figure 3. Monthly mean of OMI UV AAOD (top) at 388 nm and MERRAero simulated AAOD (middle) for July (left) and August (right) 2007. Difference of AAOD OMI minus MERRAero (bottom plots).

ACPD
14, 32177–32231, 2014

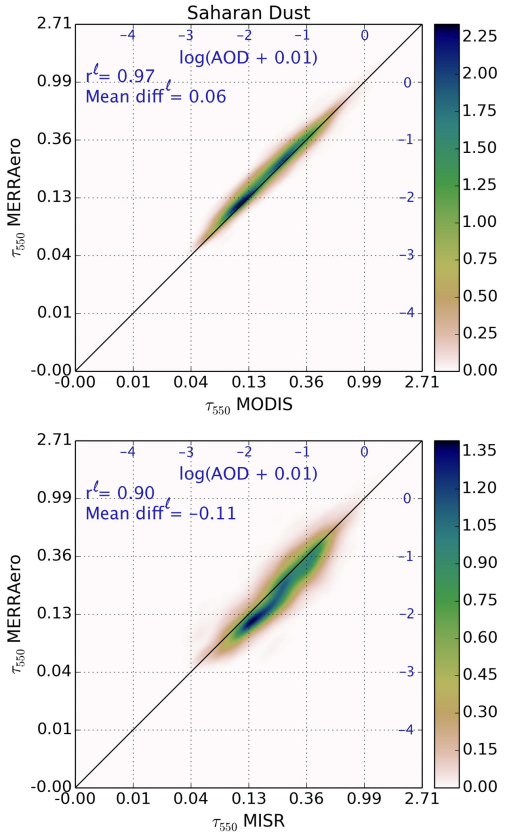

Figure 4. Comparison of 550 nm MERRAero AOD to MODIS NNR (top) and MISR (bottom) retrievals over the Saharan dust region for the period JJA 2007. r' and Mean diff$'$ are the correlation coefficient and the mean difference of the log-transformed AOD.

ACPD
14, 32177–32231, 2014

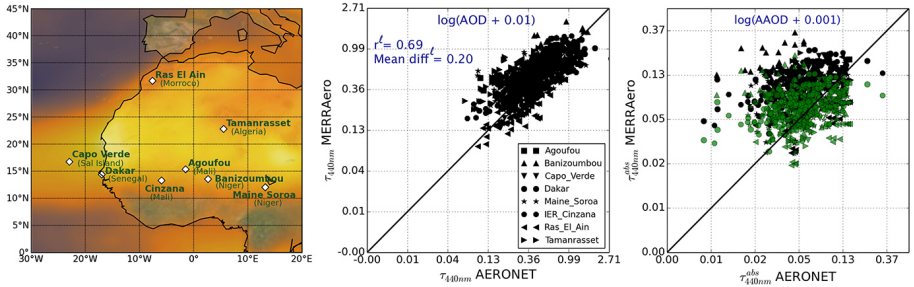

Figure 5. Comparison of MERRAero and AERONET 440 nm AOD (middle) and AAOD (right) using the OPAC dust optics in black and the observation-based dust optics in green at 8 Saharan dust AERONET sites shown on the map (left) for the period June to October 2007. The one-to-one correspondence is indicated by the black line. r' and Mean diff$'$ are the correlation coefficient and the mean difference of the log-transformed AOD.

ACPD
14, 32177–32231, 2014

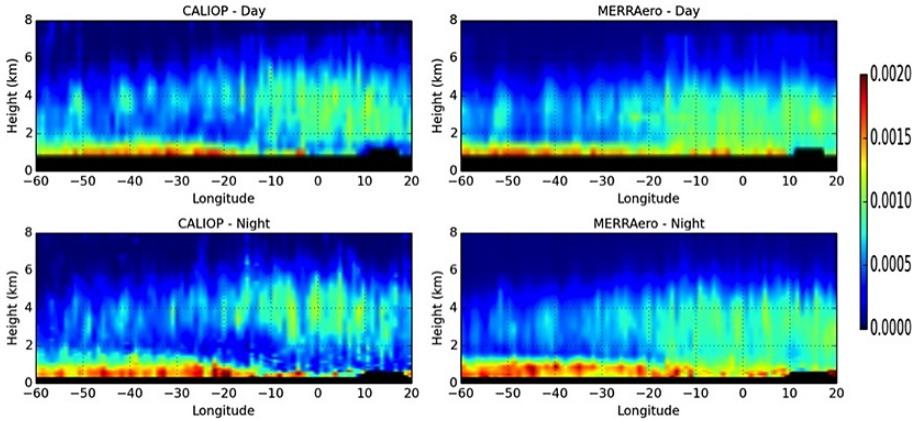

Figure 6. On the left, regional 3 months average (JJA 2007) of CALIOP attenuated backscatter coefficient ($km^{-1}\,sr^{-1}$) at 532 nm over the African dust region (60° W–20° E, 0–30° N) during the day (top) and the night (bottom). On the right, MERRAero attenuated backscatter coefficient sampled on the CALIPSO track for the same period during the day (top) and night (bottom).

ACPD
14, 32177–32231, 2014

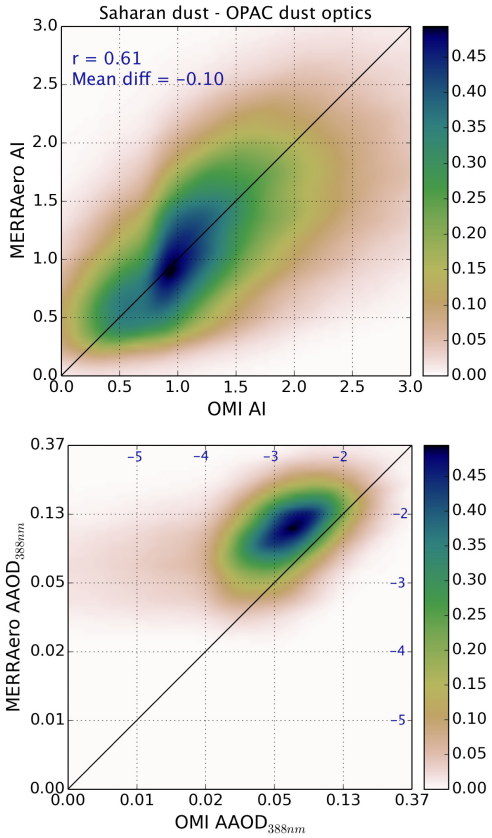

Figure 7. Comparison of MERRAero simulated AI (top) and AAOD at 388 nm (bottom) to OMI retrievals for the period JJA 2007 over the Saharan dust region. The dust OPAC optics table is used in MERRAero simulations.

ACPD
14, 32177–32231, 2014

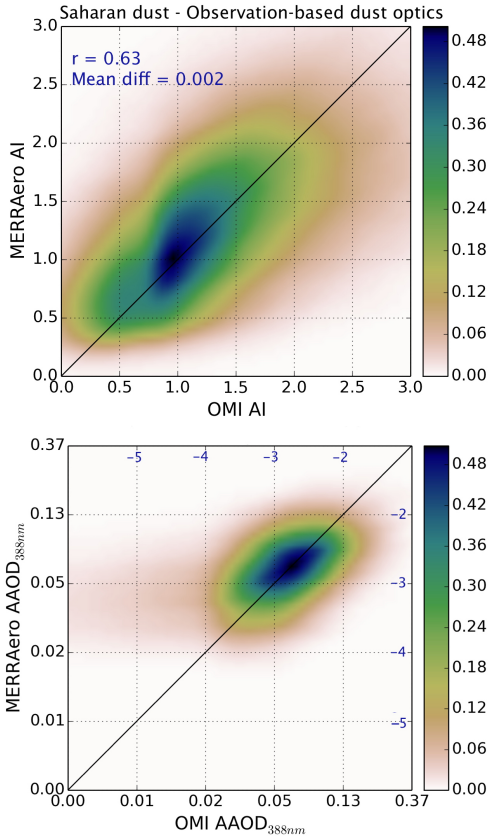

Figure 8. Same as Fig. 7 except that the dust observation-based optics table with the spectral variation of the imaginary part of the refractive index at 354 nm relative to the refractive index at 388 nm is used in MERRAero simulations.

ACPD
14, 32177–32231, 2014

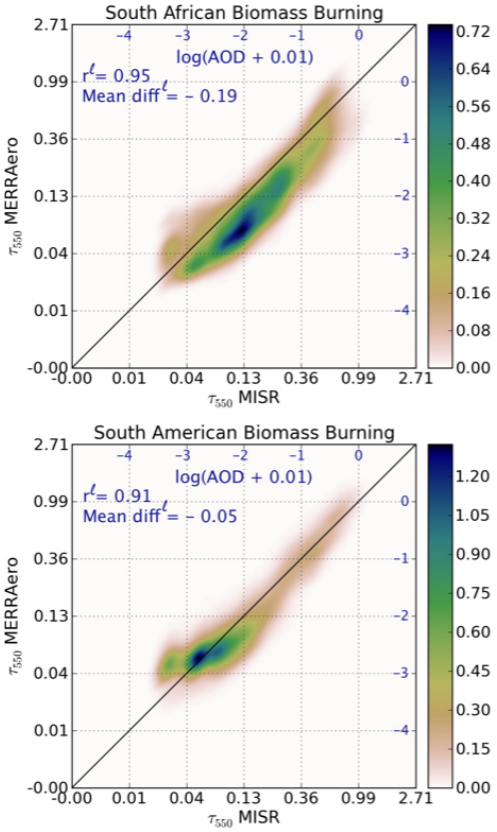

Figure 9. Comparison of 550 nm MERRAero AOD to MISR retrievals over the South African (top) and South American (bottom) biomass burning regions for the period JJA 2007.

ACPD
14, 32177–32231, 2014

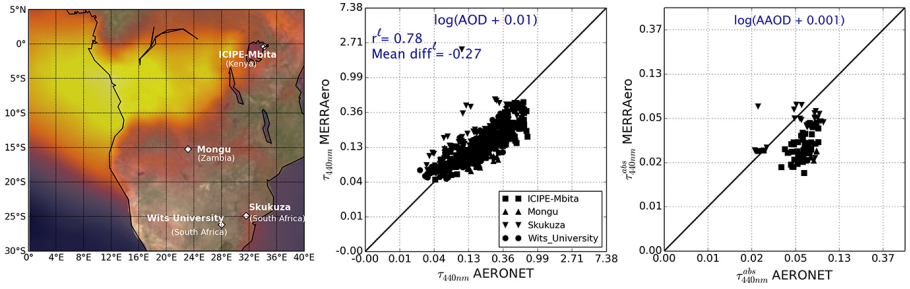

Figure 10. Same as Fig. 5 but for the south African region.

ACPD
14, 32177–32231, 2014

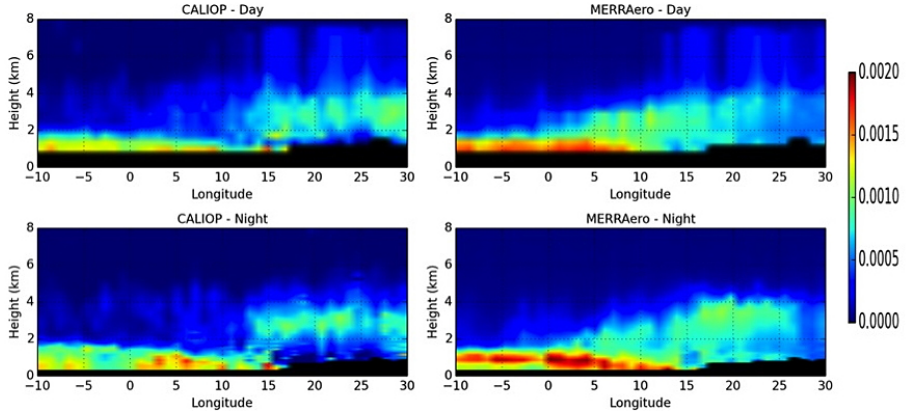

Figure 11. Same as Fig. 6 but for the South African region (10° W–30° E, 0°–30° S) during JJA 2007.

ACPD
14, 32177–32231, 2014

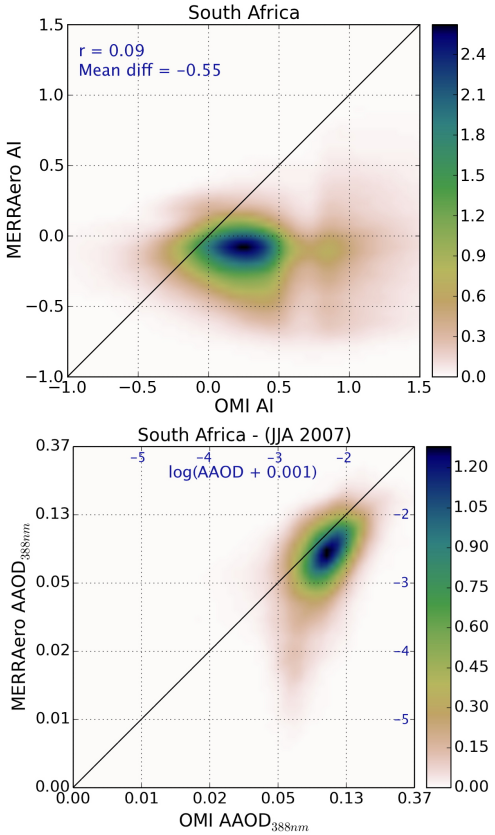

Figure 12. Comparison of MERRAero simulated AI (top) and AAOD at 388 nm (bottom) to OMI retrievals for the period JJA 2007 over the South African region.

ACPD
14, 32177–32231, 2014

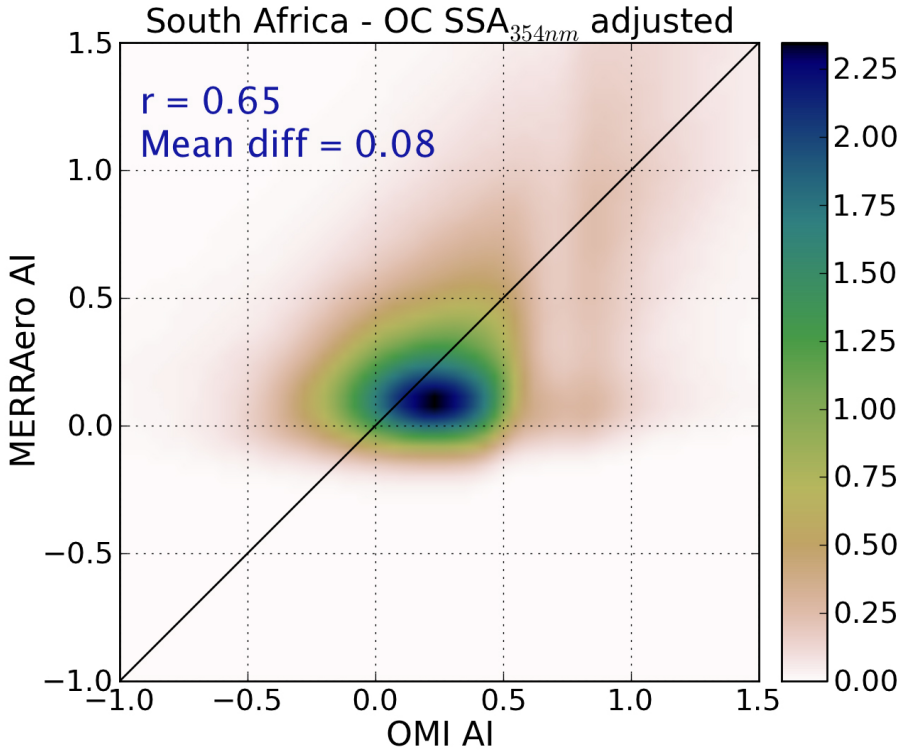

Figure 13. Comparison of AI for JJA 2007 over the south African region after decreasing the SSA at 354 nm for the organic component of biomass burning by 5 %.

ACPD
14, 32177–32231, 2014

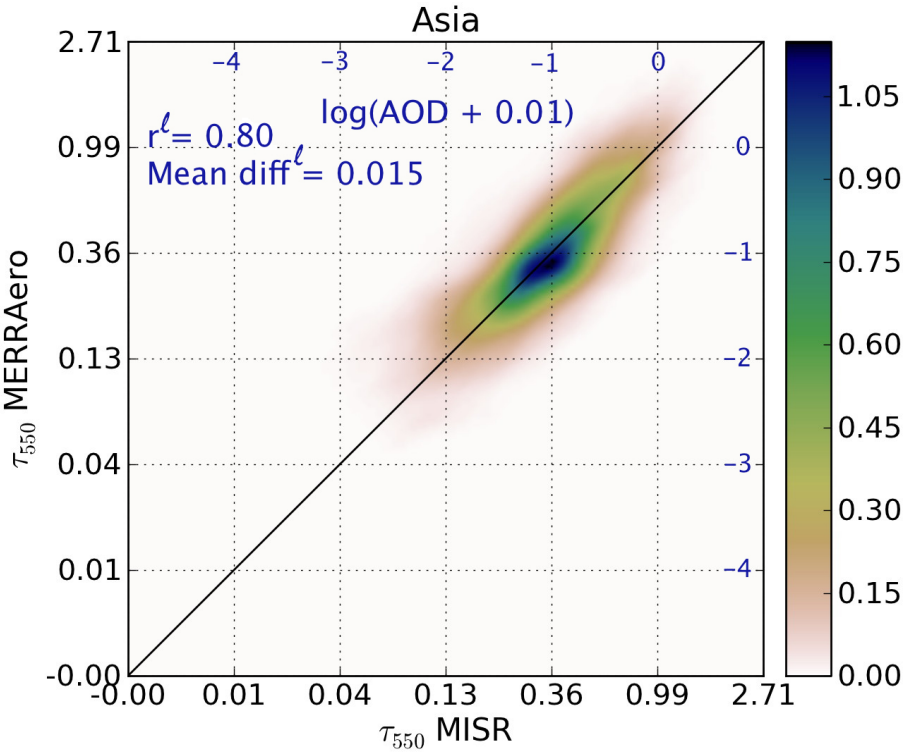

Figure 14. Same as Fig. 9 but for the Asian region during AMJ 2007.

ACPD
14, 32177–32231, 2014

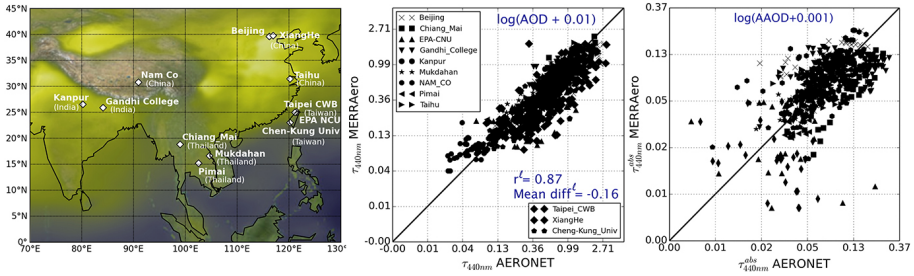

Figure 15. Same as Fig. 5 but for the Asian region.

ACPD
14, 32177–32231, 2014

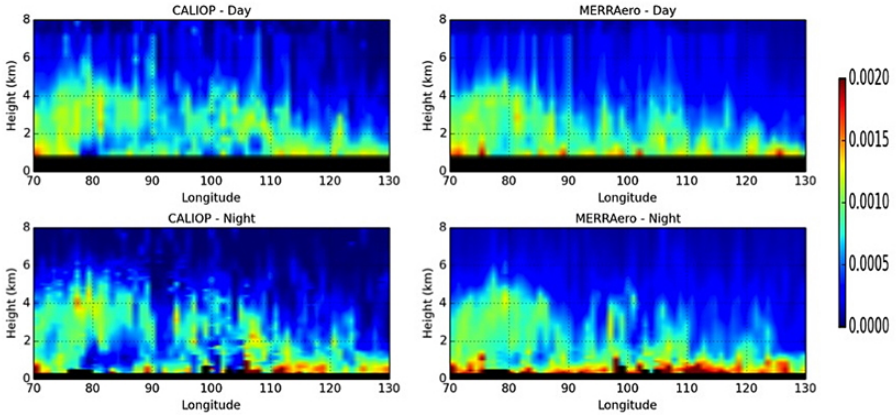

Figure 16. Same as Fig. 6. but for the Asian region (70° E–130° E, 10–40° N) during AMJ 2007.

ACPD
14, 32177–32231, 2014

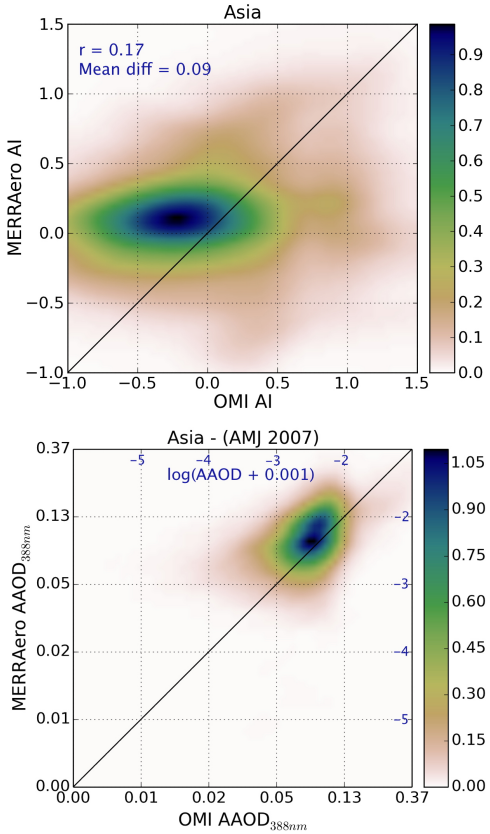

Figure 17. Same as Fig. 12 but for the Asian region during AMJ 2007.

ACPD
14, 32177–32231, 2014